PAPER

Check for updates

Facile and sustainable fabrication of transparent mesoporous IrO$_x$ films formed by nanoparticle assembly for efficient electrocatalytic water oxidation†

Debraj Chandra, [iD] ‡* Tsubasa Sato, Naoto Abe, Kenji Saito, Tatsuto Yui and Masayuki Yagi [iD] *

An efficient electrocatalyst film of iridium oxide (IrO$_x$) with low iridium usage is pivotal towards improvement of the sustainability of sparse iridium-based catalysts. A new transparent mesoporous IrO$_x$ film consisting of small interconnected nanoparticles has been developed by simple drop-casting of a homogeneous solution containing a very low concentration of a hydroxyiridate complex and a polymer surfactant Pluronic F127 followed by annealing. The intrinsic activity of catalytic Ir-sites in the mesoporous IrO$_x$-F127 film was higher than that of the IrO$_x$-untemplate film at the same annealing temperature as indicated by cyclic voltammetry. Electrochemical impedance measurements suggested faster electron transport through interconnected nanoparticles of the mesoporous network in the former film compared with the discrete nanoparticulate structure in the latter. The high intrinsic activity of Ir-sites and efficient electron transport in the novel mesoporous structure contributed to the high electrocatalytic performance observed for the IrO$_x$-F127 film annealed at 400 °C. The catalytic current of the IrO$_x$-F127 film for water oxidation with respect to the iridium amount (I_{cat}/Γ_{cov}) was 5.3 and 4.3 times higher than those of the transparent and efficient electrocatalyst films of the hitherto-reported 2D-hexagonal mesoporous IrO$_x$ (*ChemSusChem*, 2015, **8**, 795–799) and nanoparticle IrO$_x$(OH)$_y$ (*ACS Catal.*, 2016, **6**, 3946–3954), respectively.

Introduction

Recent concerns over climate change due to global warming have intensified the attention on artificial photosynthesis to develop renewable and clean energy systems for the future.[1–3] Water oxidation catalysis is a key step in photoelectrochemical[4–7] and electrochemical[8–13] water splitting to the quest of development of artificial photosynthetic devices. The critical challenge of water oxidation catalysis is to negotiate its sluggish kinetics for oxygen evolution with high efficiency.[11–15] In pursuit of this, inorganic materials of transition metal complexes and oxides have been extensively implemented and investigated in electrocatalytic water oxidation assemblies.[10–13,16–20]

Department of Materials Science and Technology, Faculty of Engineering, Niigata University, 8050 Ikarashi-2, Niigata, 950-2181, Japan. E-mail: yagi@eng.niigata-u. ac.jp; debraj.chandra@gs.niigata-u.ac.jp; Fax: +81-25-262-6790; Tel: +81-25-262-6790

† Electronic supplementary information (ESI) available. See DOI: 10.1039/c9se00731h

‡ Present address: World Research Hub Initiative (WRHI), Institute of Innovative Research, Tokyo Institute of Technology, Nagatsuta-cho 4259, Midori-ku, Yokohama 226-8503, Japan.

Iridium oxide (IrO$_x$) is an immensely important material in a variety of applications, such as catalysis,[21,22] pH sensing,[23,24] amperometric biosensing,[25] electrochromic displays[26] and electrochemical supercapacitors.[27] Such versatile applications are possible due to its high catalytic activity, actuation over a broad pH range, low resistivity and high stability under chemical/thermal treatment. So far, IrO$_x$-based nanomaterials are useful for water oxidation catalysis in both electrochemical[18,28–41] and photochemical[42–44] water splitting systems. They are especially useful for developing artificial photosynthesis, which requires high catalytic activity under neutral pH conditions because IrO$_x$ is a rare water oxidation catalyst that is able to work under neutral pH conditions. Towards the improvement of sustainability of sparse iridium-based catalysts, noteworthy efforts have been made to enhance their catalytic performance by increasing the surface area and tuning the phase/composition of nanomaterials.[33,34,37–40,45]

IrO$_x$ nanoparticle films have been predominantly utilized in electrocatalytic water oxidation assemblies because of their ease of fabrication as electrodes on various electro-conducting substrates.[18,28–35,46] IrO$_x$ nanoparticle films are obtained by particle assembly,[30–32] anodic deposition[28,34,47,48] and spin-coating[33] employing aqueous colloidal nanoparticles and

homogeneous solutions of Ir-complexes. However, in most instances of IrO_x, nanoparticle films are associated with a low/moderate surface area. Recently, mesoporous IrO_x nanostructures as electrocatalyst films have gained substantial attention due to their large internal surface area.[34–39] Several attempts have been made to prepare porous IrO_x nanostructures. The hard-template method[49] has yielded only mesoporous IrO_x powder that needs a considerable amount to be used for electrocatalyst film preparation (less sustainable).[36] The colloidal crystal template method[50] has offered only macroporous IrO_x, having a low surface area due to large void spaces.[41] Moreover, most of these reports of nanoparticles and porous IrO_x nanostructures were associated with non-transparent electrocatalyst films.[28,32,34,36,37,41] A transparent thin film is highly important for application in artificial photosynthesis (allow penetration of light to the inner photocatalyst layer, covered by the electrocatalyst[42,43]), but only a few transparent IrO_x films have been reported so far.[33,39]

Surfactant-templating strategies have been widely acceptable for fabrication of transparent mesoporous metal oxide films.[39,51,52] Surfactant-templated porosity has been reported for a few non-transparent IrO_x films prepared by the dip-coating method,[37,38] in which connectivity between the obtained spherical mesopores (>15 nm) could be a critical issue.[53,54] We recently demonstrated that a transparent 2D-hexagonal mesoporous IrO_x electrocatalyst film for water oxidation was prepared using a triblock copolymer surfactant, "Pluronic F127" ($EO_{106}PO_{70}EO_{106}$; EO and PO represent poly(ethylene oxide) and poly(propylene oxide) units, respectively) by means of a spin-coating technique followed by annealing.[39] Actually, the film provided a high specific surface area up to 105 $m^2 g^{-1}$. However, the observed catalytic current for water oxidation with respect to the iridium amount should be improved. Due to the formation of relatively thick (≈ 5 nm) pore-walls around large cylindrical pores (≈ 7 nm) in 2D-hexagonal mesoporous IrO_x, electrocatalytic activity with respect to the iridium amount is not satisfactory.[39] Moreover, the spin-coating technique unnecessarily wastes precious iridium since the precursor solution is perfused from the substrate. At the present stage, development of surfactant-templated IrO_x nanostructures as efficient electrocatalyst films with low iridium usage is a difficult and challenging goal. We explore the possibility of such novel IrO_x nanostructures by considering the flexible role of Pluronic F127 as a template due to the small difference in hydrophobicity between its EO and PO units.[51,55,56] Our aim is to develop a simple and sustainable method for fabrication of an efficient transparent IrO_x electrocatalyst film with low iridium usage. Herein, we report facile fabrication of a new mesoporous IrO_x film formed by assembly of small interconnected nanoparticles (ca. 2–5 nm). A transparent amorphous IrO_x coating layer was obtained by simple drop-casting of a homogeneous solution having a very low concentration of a hydroxyiridate complex with Pluronic F127 followed by annealing. The unique mesoporous structure of the amorphous IrO_x film prominently improves the performance for water oxidation with respect to the iridium amount compared to the transparent and efficient

electrocatalyst films of hitherto-reported 2D-hexagonal mesoporous IrO_x[39] and nanoparticle $IrO_x(OH)_y$.[33]

Results and discussion

Preparation and physicochemical characterization

In the presence of Pluronic F127, the aqueous precursor solution is homogeneous (Fig. 1a) and stable for at least several days at room temperature. The absence of any preformed colloidal and/or nanoparticle species in the precursor solution was verified by dynamic light scattering (DLS) measurements. The stable precursor solution can be obtained under the employed synthesis conditions, in which basic hydrolysis was proceeded by a lower amount of NaOH ($NaOH/K_2IrCl_6$ mole ratio of 1.93) than the stoichiometric requirement for hydrolysis of six chloride ions of K_2IrCl_6 ($NaOH/K_2IrCl_6$ mole ratio should be 6.0). The higher amount of NaOH gradually increased the possibility of formation of colloidal particles and finally produced a black precipitate in 0.5–24 h. The precursor solution is most likely composed of various partially hydrolyzed $[Ir(OH)_x(OH_2)_yCl_z]^{n-}$ complex species.[33] The coating layer deposited over FTO electrodes from this precursor solution is highly transparent (Fig. 1a). The transmission spectrum of the present IrO_x-F127 electrode was nearly the same as that of the bare FTO electrode (Fig. S1†). The coverage (Γ_{cov}) of deposited Ir-species is 5.2 ± 0.4 nmol cm^{-2} under employed conditions (Γ_{cov} estimated from the iridium amount measured by an ICP-AES technique), which could be controlled by varying the amount of the drop-cast solution. The Raman spectrum (Fig. S2†) of the as-prepared precursor film showed signals at 168, 285, 315 and 335 cm^{-1} assigned to the Ir–OH moieties of $[Ir(OH)_x(OH_2)_yCl_z]^{n-}$ complex species.[33] When the film was calcined at 400 °C (under N_2 followed by under O_2), the Ir–OH signals completely disappeared and a broad intense band at 516 cm^{-1} and weak bands at 302 and 713 cm^{-1} were observed in agreement with formation of amorphous IrO_x.[57,58] Specific bands assigned to the E_g, B_{2g} and A_{1g} phonon bands of crystalline IrO_2 at 559, 729 and 746 cm^{-1}, respectively were observed at 450 °C and became more resolved at 500 °C.[59–61] The Raman spectrum of a control IrO_x-F127 film annealed at 400 °C under N_2 (Fig. S3a†) exhibited two additional broad bands around 1362 and 1590 cm^{-1} attributed to amorphous carbon,[7,62,63] which completely disappeared after calcination at 400 °C under O_2. These carbonaceous species could provide better stability during formation of the mesoporous structure rather than direct calcination under O_2.[7,63] The signals at 228, 362, 537, 845 and 930 cm^{-1} for Pluronic F127 diminished completely over 400 °C, indicating its decomposition. This is in agreement with the FTIR spectrum (Fig. S4†), which shows that C–H stretching vibration bands at 2925 cm^{-1} (asymmetric) and 2874 cm^{-1} (symmetric) observed for Pluronic F127 in the as-prepared film have disappeared in the film calcined at 400 °C.

The SEM images (Fig. 1b) of a representative IrO_x-F127 film calcined at 400 °C revealed different aspects of the deposited layer on the FTO surface. A large domain of the FTO surface was observed to be covered by a thin coating layer of deposited Ir-species over a scale of several micrometers. However,
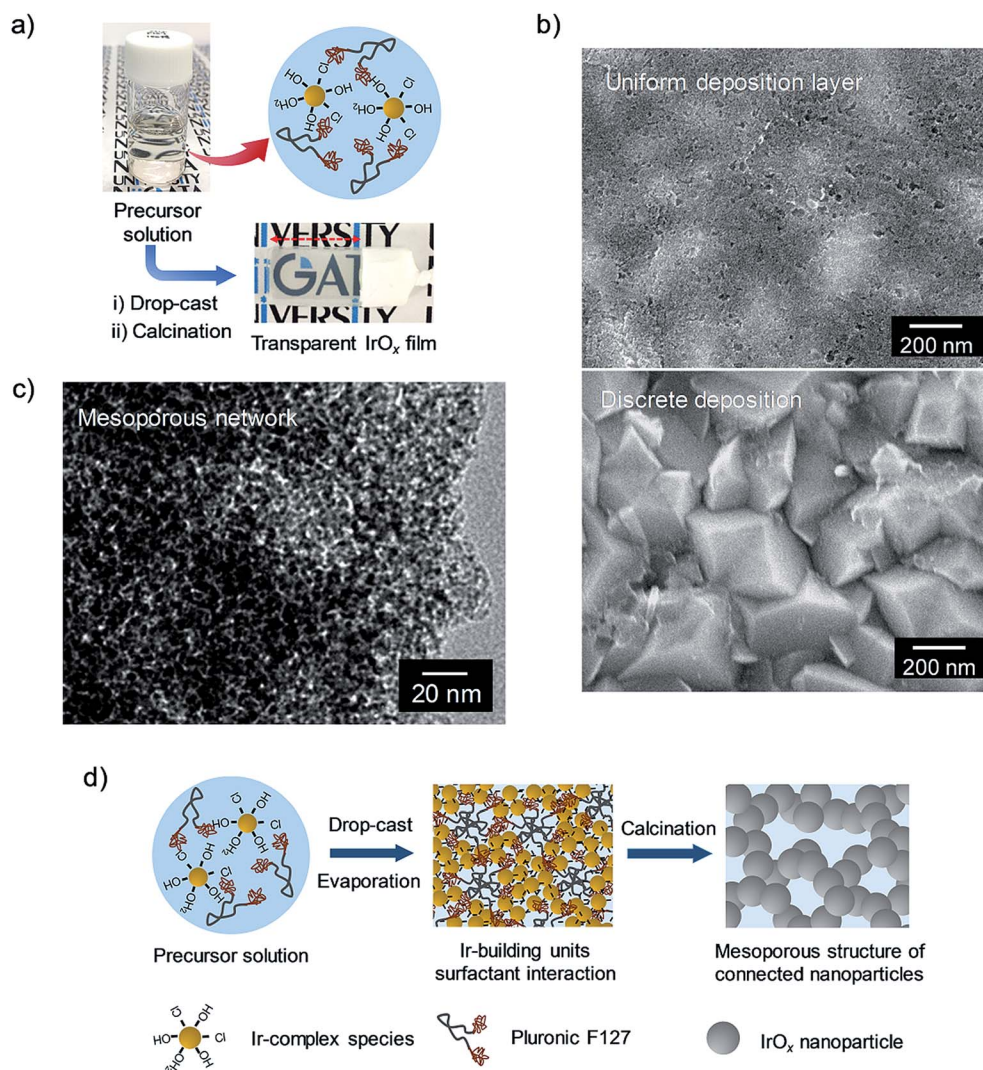
Fig. 1 (a) Formation route of the transparent IrO$_x$-F127 film illustrated by photographs. The film is calcined at 400 °C. (b) SEM images of the IrO$_x$-F127 film calcined at 400 °C. (c) TEM image of the IrO$_x$-F127 film calcined at 400 °C. (d) Conceptual schematic illustration for the formation of the mesoporous network of interconnected IrO$_x$ nanoparticles.

a significant fraction of the uneven FTO surface was uncovered except for the presence of a few discrete deposits, which is primarily attributed to the lower Γ_{cov} (5.2 ± 0.4 nmol cm^{-2}) of Ir-species compared to our previous report of the 2D-hexagonal mesoporous IrO$_2$ film (Γ_{cov}, ~30 nmol cm^{-2}) obtained by a spin coating method.[39] A higher fraction of the deposited layer of Ir-species was observed with a gradual increase of Γ_{cov} by repeated drop-casting. The TEM image (Fig. 1c) of the IrO$_x$-F127 film calcined at 400 °C showed the presence of low electron density spots (pores) throughout the specimen, and a disordered arrangement of mesopores of ≤5 nm is quite clear. A close look at the HRTEM image (Fig. S5†) revealed that the assembly of finely distributed and well-connected nanoparticles (*ca.* 2–5 nm) is composed of the framework of the mesoporous nanostructure. In contrast, the TEM image of the IrO$_x$-untemplate film (Fig. S6†) shows discrete nanoparticles (*ca.* 2–5 nm). Moreover, the nanoparticles partially became aggregated to form large secondary particles (≥15 nm).

The small-angle XRD patterns (Fig. 2a) of the IrO$_x$-F127 films calcined at 400 and 450 °C showed single diffraction peaks at 0.84 and 0.96 degrees, respectively, suggesting the formation of nanostructured IrO$_x$ materials with no long range mesoscopic ordering. The *d*-spacing values (pore-center to pore-center average distance) calculated from XRD peaks are 10.5 and 9.1 nm at 400 and 450 °C, respectively. However, the peak disappeared in the XRD pattern of the film calcined at 500 °C, depicting degradation of the mesostructure. No XRD peak was detected for the IrO$_x$-untemplate film, suggesting no mesostructure was formed without Pluronic F127 in the precursor solution. An amorphous phase of the IrO$_x$ framework was detected up to 400 °C from the wide angle XRD patterns (Fig. 2b) of the IrO$_x$-F127 film, which is crystallized to a tetragonal phase of IrO$_2$ (JCPDS: 150870) after calcination over 450 °C. The average crystallite sizes of about 4.6 and 8.1 nm at 450 and 500 °C, respectively, were estimated from the [101] plane using the Scherrer equation and assuming a Scherrer constant of 0.94,
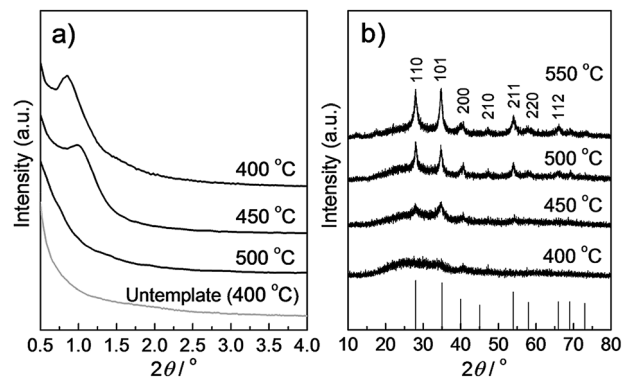
Fig. 2 Small-angle (a) and wide-angle (b) XRD patterns of the IrO_x-F127 samples calcined at 400–550 °C. Gray line shows the small-angle XRD pattern of the IrO_x-untemplate sample calcined at 400 °C. Reference JCPDS pattern for the wide-angle XRD is shown by vertical drop lines.

which suggests gradual growth of the nanoparticles consisting of the mesoporous network through crystallization at higher temperatures. This is responsible for the collapse of the mesoporous structure at 500 °C.

The N_2 sorption isotherm of a representative IrO_x-F127 sample (Fig. 3a) calcined at 400 °C depicted a type-IV curve, being characteristic of mesoporous materials.[55,64] N_2 uptake of the mesopores through a capillary condensation step occurred by a gradual increase of the adsorption amount above relative pressure $(P/P_0) \approx 0.15$. H2-type hysteresis loops could be related to the roughness of the surfaces of nanoparticles comprising the mesoporous network.[65] The pore size distribution (Fig. 3b) showed a peak pore width at 4.1 nm, agreeing well with those values obtained from TEM analyses. The BET surface area and mesopore volume are calculated to be 75 m^2 g^{-1} and 0.25 cm^3 g^{-1}, respectively. Considering the high density of the crystalline IrO_2 (11.66 g cm^{-3}; tetragonal phase) compared with silica, the BET surface area of the mesoporous IrO_x-F127 is comparable with that of the block copolymer templated ordered mesoporous silica.[56,64] These are in contrast to the data of IrO_x-

untemplate, showing a significantly low adsorption amount up to $P/P_0 \approx 0.8$ due to the discrete nanoparticulate structure and a sharp N_2 uptake above $P/P_0 \approx 0.9$ attributed to the adsorption in void spaces between large secondary particles (as observed in the TEM image). Accordingly, the IrO_x-untemplate film yielded a lower BET surface area of 21 m^2 g^{-1} but a pore volume of 0.23 cm^3 g^{-1} comparable to those of IrO_x-F127.

As indicated by the results of the above physicochemical characterization techniques, Pluronic F127 has strongly influenced the nanostructural properties of the IrO_x-F127 film. The formation mechanism of the nanostructure in the IrO_x-F127 film is illustrated in Fig. 1d. The strong interaction between the partially hydrolyzed $[Ir(OH)_x(OH_2)_yCl_z]^{n-}$ complex species and hydrophilic EO blocks of Pluronic F127 is responsible for a stable homogeneous precursor solution,[39,40] which assists micelle formation in a mesoscopic orientation during the evaporation-induced self-assembly (EISA) process[51,52,66] by drop-casting. Ir-building-units interacting closely with hydrophilic EO-blocks on the surface of the formed micelles undergo gradual condensation during calcination to produce interconnected small IrO_x nanoparticles (*vide supra*), though mesopores were formed by the void space created from burned out micelles. The polymeric EO chains surrounding the Ir-building-units inhibit the aggregation of nanoparticles during calcination. The absence of Pluronic F127 in the IrO_x-untemplate film caused discrete nanoparticles, which became aggregated in a large fraction during calcination.

Electrocatalytic properties

Influence of the mesoporous structure towards high electrocatalytic activity. Electrocatalytic water oxidation using the IrO_x-F127 electrodes was carried out under neutral conditions (0.1 M phosphate solution, pH $\approx$ 7.0) allowing for application in artificial photosynthesis. The cyclic voltammogram (CV) in the potential range from 0 to 0.9 V for the IrO_x-coated electrodes calcined at 400 °C exhibits broad anodic peaks at $\approx$0.25 V and $\approx$0.55 V (Fig. 4a), assigned to oxidation of Ir^{III}/Ir^{IV} and Ir^{IV}/Ir^{V} redox pairs of the IrO_x, respectively.[28,31] The capacitive current is
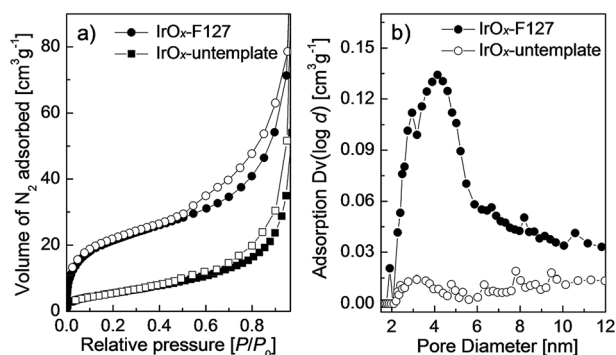

Fig. 3 N_2 sorption isotherms (a) and pore size distributions (b) of IrO_x-F127 and IrO_x-untemplate samples calcined at 400 °C. In N_2 sorption isotherms adsorption and desorption points are marked by closed and open symbols respectively.

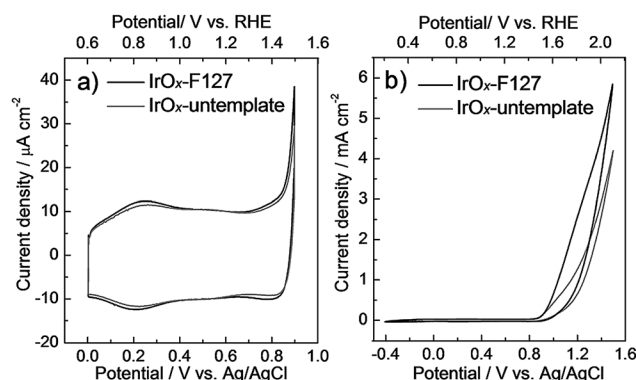**Fig. 4** Cyclic voltammograms of IrO_x-F127 and IrO_x-untemplate electrodes annealed at 400 °C as measured in a 0.1 M phosphate solution (pH $\approx$ 7.0) in potential windows (a) between 0 and 0.9 V and (b) between −0.4 and 1.5 V *vs.* Ag/AgCl.

Table 1 Electrochemical properties of different IrO_x electrodes annealed at 400–550 °C as measured in a 0.1 M phosphate solution (pH ≈ 7.0)

Sample name	Calcination temp [°C]	Γ_{ea}[a]	I_{cat} [mA cm^{-2}]	A_{cat}[b]	η[c] [V]	Tafel slope [mV dec^{-1}]
IrO_x-untemplate	400	0.96	4.2	0.75	0.31	51
IrO_x-F127	400	1	5.8	1	0.30	45
IrO_x-F127	450	0.87	2.6	0.51	0.38	56
IrO_x-F127	500	0.59	1.0	0.29	0.50	62
IrO_x-F127	550	0.38	0.4	0.19	0.66	83

[a] Γ_{ea} (relative amount of electroactive Ir) was calculated from the integrated anodic current between 0.05 and 0.80 V of CV. [b] A_{cat} (relative intrinsic catalytic activity of Ir-sites) was defined as I_{cat} normalized by Γ_{ea} and expressed as relative values to "IrO_x-F127" calcined at 400 °C. [c] η is the overpotential for water oxidation and was calculated from the difference between the onset potential and the theoretical potential (0.618 V vs. Ag/AgCl at pH = 7.0, corresponding to 1.23 V vs. RHE) for water oxidation. The onset potentials were taken as the potentials to reach the current density of 200 μA cm^{-2}.

insignificant compared with the Ir redox-based current in this potential range for the IrO_x-F127 films with very low Γ_{cov} (5.2 ± 0.4 nmol cm^{-2}) of Ir-species.[33,40] Due to the fused Ir^{III}/Ir^{IV} and Ir^{IV}/Ir^{V} redox pairs (Fig. 4a) it is difficult to reliably analyze the amount of electroactive Ir-sites. Nevertheless, the relative amounts (Γ_{ea}) of electroactive Ir-sites were estimated from the total anodic current area from 0.05 to 0.80 V as described similarly in previous reports.[33,40] The Γ_{ea} value for IrO_x-F127 (1.0) is a little higher relative to IrO_x-untemplate (0.96) (Table 1) annealed at 400 °C, which suggests only minor enhancement of the electroactivity of the Ir-sites by the mesoporous structure. This is inconsistent with the enhancement (3.6 times) of the specific surface area by the mesoporous structure (75 and 21 m^2 g^{-1} for IrO_x-F127 and IrO_x-untemplate, respectively). This could be explained by the permeation of electrolytes through the mesoporous network (different from physisorption of N$_2$ gas) for the IrO_x-F127 film.

The CV in the wide potential range from −0.4 to 1.5 V concurrently showed anodic current due to water oxidation above ≈ 0.88 V (Fig. 4b). The catalytic current density (I_{cat}) at 1.5 V of the IrO_x-F127 (5.8 mA cm^{-2}) was 1.4 times higher than that of the IrO_x-untemplate (4.2 mA cm^{-2}), although both the electrodes have the same Γ_{cov} (5.2 ± 0.4 nmol cm^{-2}) of Ir atoms. The normalized I_{cat} value (1.11 mA nmol^{-1}) at 1.5 V by Γ_{cov} (given as I_{cat}/Γ_{cov}) for the IrO_x-F127 (I_{cat} = 5.8 mA cm^{-2}, Γ_{cov} = 5.2 ± 0.4 nmol cm^{-2}) was 5.3 and 4.3 times higher than those for the hitherto-reported efficient electrocatalyst films of 2D-hexagonal mesoporous IrO_x[39] (0.21 mA nmol^{-1}: I_{cat} = 6.2 mA cm^{-2}, Γ_{cov} = ~30 nmol cm^{-2}) and nanoparticle $IrO_x(OH)_y$[33] (0.26 mA nmol^{-1}: I_{cat} = 9.9 mA cm^{-2}, Γ_{cov} = 38 ± 0.6 nmol cm^{-2}), respectively. However, the I_{cat} value for the IrO_x-F127 increased almost linearly up to 10.4 nmol cm^{-2}, and thereafter I_{cat} gradually reached saturation at higher Γ_{cov} due to the restricted accessibility of the catalytic-sites to the electrolyte solution (Fig. S7†). Even at a similar Γ_{cov} (~31 nmol cm^{-2}), the normalized I_{cat} value (0.39 mA nmol^{-1}) by Γ_{cov} for the IrO_x-F127 (I_{cat} = 12.0 mA cm^{-2}, Γ_{cov} = ~31 nmol cm^{-2}) was 1.9 times higher than that for the 2D-hexagonal mesoporous IrO_x.[39] These show that it is possible to create a highly efficient IrO_x electrocatalyst film with low iridium usage by simple drop-casting employing a surfactant-templating strategy.

The overpotential (η/V) for the IrO_x-F127 calcined at 400 °C was calculated from the onset potential that was defined as the potential for the catalytic current generation at 200 μA cm^{-2}. The η value was significantly low (0.30 V) (Table 1), which is fairly close to those of some most efficient electrocatalysts (η = 0.20–0.25 V) including nanoparticle-IrO_x[28,29,33,34] and surfactant templated mesoporous-IrO_x[37–39] electrodes. The I_{cat} value normalized by Γ_{ea} is denoted as the relative intrinsic activity (A_{cat} = I_{cat}/Γ_{ea}) of Ir-sites for electrocatalytic water oxidation (Table 1). The A_{cat} value for IrO_x-F127 was higher than that (25% loss) for IrO_x-untemplate at the same coverage (Γ_{cov} = 5.2 ± 0.4 nmol cm^{-2}) and annealing temperature (400 °C). The increase of the observed I_{cat} value of IrO_x-F127 can be explained by the increase of intrinsic activity of the Ir-sites rather than the increase of the number of Ir-sites. This is a contrast to the case of the pervious 2D-hexagonal mesoporous IrO_x system;[39,40] the observed I_{cat} value was increased by not the increase of the intrinsic activity of the Ir-sites (nearly the same A_{cat} value) but the increase of the number of Ir-sites (Γ_{ea} value increased by 2D-hexagonal mesoporous structure). The higher intrinsic activity of the Ir-sites for the IrO_x-F127 electrode could be caused possibly by finely distributed and well-connected nanoparticles (ca. 2–5 nm) compared with the nanoparticles partially aggregated to form large secondary particles (≥15 nm) for IrO_x-untemplate.
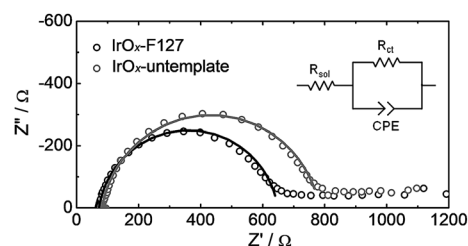

Fig. 5 Nyquist plots of IrO_x-F127 and IrO_x-untemplate electrodes annealed at 400 °C as measured in a 0.1 M phosphate solution (pH ≈ 7.0) at 1.0 V vs. Ag/AgCl. The solid lines show simulated spectra by fitting to the impedance data in a frequency region of 1 mHz to 20 kHz using equivalent circuits (inset). R_{ct}, R_{sol} and CPE are charge transfer resistance, solution phase resistance and constant phase element, respectively.

Electrochemical impedance measurements were performed to assess the electron transport and its impact on electrocatalytic properties. Nyquist plots of the IrO_x-F127 and IrO_x-untemplate electrodes showed semicircles in a high frequency region and subsequent flat plots in a low frequency region (Fig. 5). For analysis of the Nyquist plots the high frequency region was used by considering an equivalent circuit comprising solution phase resistance (R_{sol}), charge transfer resistance (R_{ct}), and constant phase element (CPE) (see the inset of Fig. 5) because analysis of the flat plots in a low frequency region (representing a relatively slow kinetic process) circuit is complicated. The given parameters of the elements of the equivalent circuits are summarized in Table 2. The CPE constant (T_{CPE}), related to electric double layer capacitance, does not vary considerably for IrO_x-F127 (152 mF $s^{(p-1)}$) and IrO_x-untemplate (164 mF $s^{(p-1)}$) (p values are the same (0.90)), which is consistent with the little enhancement of electroactivity of the Ir-sites by the mesoporous structure. The R_{ct} value for IrO_x-F127 (576 Ω) was significantly lower than that for IrO_x-untemplate (700 Ω), signifying that electron transport in the former film is faster than that in the latter. The faster electron transport in the former film could be attributed to the well-interconnected nanoparticles of the mesoporous network compared with the discrete nanoparticulate structure of the latter (*vide supra*).

Impact of calcination temperature on the electrocatalytic activity of mesoporous IrO_x electrodes. Fig. 6a shows the CV in the potential range from 0 to 0.9 V for the IrO_x-F127 electrodes calcined at 400–550 °C. The Γ_{ea} values (estimated from the entire anodic current area from 0.05 to 0.80 (ref. 33 and 40)) are variable by a factor of 0.38–1.0 among the 400–550 °C-annealing films despite the same coverage ($\Gamma_{cov} = 5.2 \pm 0.4$ nmol cm^{-2}) of Ir atoms (Table 1). The gradual decrease of Γ_{ea} with an increase of annealing temperature from 400 to 550 °C is attributed to the formation of large crystalline particles in the depleted mesoporous network at higher temperatures as confirmed by XRD analysis,[33] while the CV in the wide potential range from −0.4 to 1.5 V (Fig. 6b) showed the highest I_{cat} of 5.8 mA cm^{-2} at 1.5 V at 400 °C annealing, which noticeably decreased at higher temperatures (Table 1). Consequently, the A_{cat} value at 400 °C annealing was 2.0–5.3 times higher than those for the other calcination temperatures (Table 1), which indicates that the intrinsic catalytic activity of the Ir-sites in the amorphous IrO_x
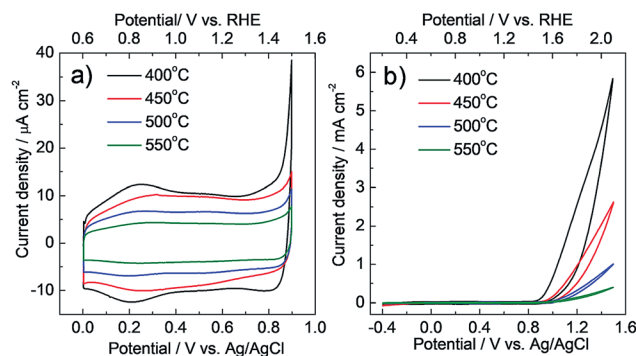

Fig. 6 Cyclic voltammograms of IrO_x-F127 electrodes annealed at 400–550 °C as measured in a 0.1 M phosphate solution (pH $\approx$ 7.0) in potential windows (a) between 0 and 0.9 V and (b) between −0.4 and 1.5 V *vs.* Ag/AgCl.

(400 °C) is higher compared with that in crystalline IrO_2 (450–550 °C) in the mesoporous film when taking characterization by the XRD and Raman spectral data into account (*vide supra*). This shows that the decrease of I_{cat} at higher calcination temperatures is explained not only by the collapse of the mesoporous structure but also by the decreased intrinsic activity of the Ir-sites due to the formation of large crystalline particles. The high intrinsic activities of the Ir-sites along with the superior mesoporous structure are responsible for high I_{cat} for the IrO_x-F127 film calcined at 400 °C.

Fig. 7 shows the Tafel plots of the IrO_x-F127 electrodes, measured based on water oxidation to characterize the IrO_x electrocatalyst,[28,47,67] and the corresponding Tafel slopes are listed in Table 1. Tafel plots depended on annealing temperature; the lowest Tafel slope was obtained as 45 mV dec^{-1} at 400 °C and it gradually increased at higher temperatures (Table

Table 2 Parameters of the elements of R_{sol}, R_{ct} and CPE in the equivalent circuit (inset of Fig. 6) for IrO_x-F127 and IrO_x-untemplate electrodes annealed at 400 °C[a]

Sample name	R_{sol}/Ω	R_{ct}/Ω	CPE T_{CPE}[b]/mF $s^{(p-1)}$	p[c]
IrO_x-F127	72	576	152	0.90
IrO_x-untemplate	82	700	164	0.90

[a] Impedance data were taken at 1.0 V *vs.* Ag/AgCl. The parameters are given by fitting to the impedance data in a frequency region of 1 mHz to 20 kHz. [b] T_{CPE} is a CPE constant. [c] p is a CPE exponent of non-ideality.
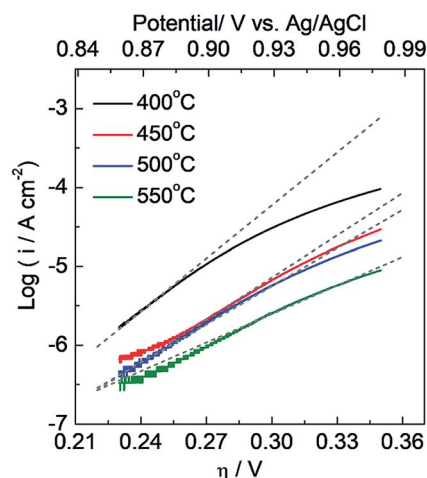

Fig. 7 Tafel plots of IrO_x-F127 electrodes annealed at 400–550 °C for electrocatalytic water oxidation as measured in a 0.1 M phosphate solution at pH = 7.0. η is an overpotential for water oxidation and calculated from the difference between the applied potential and the theoretical potential (0.618 V *vs.* Ag/AgCl at pH = 7.0, corresponding to 1.23 V *vs.* RHE) for water oxidation.
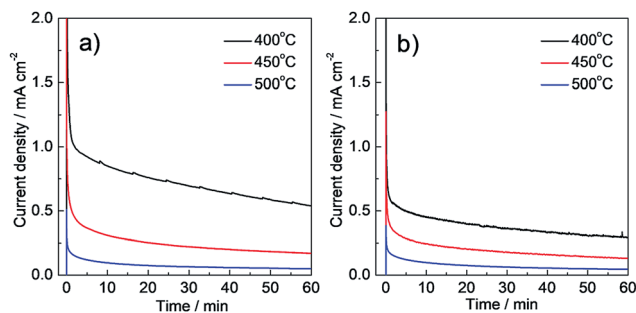
Fig. 8 Current–time profiles during electrocatalysis using (a) IrO$_x$-F127 and (b) IrO$_x$-untemplate electrodes annealed at 400–500 °C as measured in a 0.1 M phosphate solution (pH $\approx$ 7.0) at 1.2 V *vs.* Ag/AgCl.

1). This is consistent with the CV measurement revealing lowered I_{cat} for water oxidation at elevated annealing temperature. The Tafel slope for the IrO$_x$-untemplate (51 mV dec^{-1}) is significantly higher than that for the IrO$_x$-F127 under the same annealing conditions of 400 °C. The Tafel slope for the IrO$_x$-F127 electrode obtained at 400 °C is comparable with those ($\approx$ 40–50 mV dec^{-1}) of some hitherto-reported efficient electrocatalysts of IrO$_x$ nanoparticle films[28,33] and markedly lower than most other reports (60–130 mV dec^{-1}) of IrO$_x$ nanostructures.[47,68,69]

Bulk electrocatalysis performance for water oxidation. Bulk electrolysis was also conducted under potentiostatic conditions to evaluate the performance of different IrO$_x$ electrodes for electrocatalytic water oxidation. Fig. 8a displays the current–time profiles during bulk electrolysis employing IrO$_x$-F127 electrodes annealed at different temperatures. An anodic current due to electrocatalytic water oxidation was observed (after the initial spike) for the corresponding IrO$_x$ electrodes. The amorphous IrO$_x$-F127 electrode calcined at 400 °C (denoted by A_{cat} in CV measurements and mesostructural properties) provides superior electrocatalytic performance, resulting in the highest charge amount passed (2.61C) and the amount (n_{O_2}) of O$_2$ evolved (6.7 μmol, 100% faradaic efficiency (F.E.$_{O_2}$)) (Table 3). The n_{O_2} value was 3.0 and 9.6 times higher

than those of the crystalline IrO$_x$-F127 electrodes calcined at 450 °C (2.2 μmol, 95% F.E.$_{O_2}$) and 500 °C (0.7 μmol, 99% F.E.$_{O_2}$), respectively (Table 3). The current–time profiles during bulk electrolysis of IrO$_x$-untemplate electrodes annealed at different temperatures are displayed in Fig. 8b. The enhancement effect (defined as $R_{mes} = n_{O_2}$ for IrO$_x$-F127/n_{O_2} for IrO$_x$-untemplate) of the mesoporous structure for the amorphous IrO$_x$ electrode obtained at 400 °C is R_{mes} = 1.9 (Table 3). However, the R_{mes} values (R_{mes} = 1.3 and 1.0 at 450 and 500 °C, respectively) gradually decreased at higher calcination temperatures, consistent with the more prominent degradation of the mesoporous structure at 500 °C (see XRD analysis). These results clearly demonstrate that the mesoporous structure of interconnected IrO$_x$ nanoparticles enhances the electrocatalytic performance for water oxidation. The higher performance is ascribed to the high intrinsic catalytic activity of Ir-sites (high A_{cat}) and efficient electron transport in the IrO$_x$ film (low R_{ct}).

During the bulk electrolysis for all the IrO$_x$ electrodes the catalytic current density decreased by 45–51% with time from 1.5 minutes to 1 h (Fig. 8). The current density decrease was 52% during the electrolysis extended to 5 h (using the different sample of the IrO$_x$-F127 electrode calcined at 400 °C, Fig. S8†). However, here the decreased current density is not ascribed to the collapse of the mesoporous structure of the IrO$_x$-F127 electrode because 90% and 86% of the charge amount passed in the first bulk electrolysis (2.61C) have been recovered in the second (2.34C) and third (2.25C) trials, respectively (Fig. S9† and Table 3). This suggests that the mesoporous structure of the IrO$_x$-F127 electrode is basically retained during the electrolysis. An increase of the local proton concentration close to the mesoporous catalyst surface by the course of water oxidation (2H$_2$O → O$_2$ + 4H$^+$ + 4e$^-$) is primarily responsible for the decrease of the current density with time, which makes water oxidation thermodynamically unfavorable. However, due to the elution or deactivation of the catalyst ca. 10–14% loss of the charge amount for water oxidation could have resulted in the second and third trials, respectively.

Table 3 Summary of data on electrocatalytic water oxidation at 1.2 V *vs.* Ag/AgCl for 1 h in a 0.1 M phosphate solution (pH $\approx$ 7.0) using different IrO$_x$ electrodes annealed at 400–550 °C

Sample name	Calcination temp (°C)	Charge/C	n_{O_2}/μmol	F.E.$_{O_2}$[a] (%)	n_{H_2}[b]/μmol	F.E.$_{H_2}$[c] (%)	R_{mes}[d]
IrO$_x$-F127	400	2.61	6.7	100	13.2	97	1.9
IrO$_x$-F127[e]	400	2.34	6.1	100	12.0	99	
IrO$_x$-F127[f]	400	2.25	5.7	99	11.3	98	
IrO$_x$-F127	450	0.90	2.2	95	4.3	92	1.3
IrO$_x$-F127	500	0.27	0.7	99	1.4	100	1.0
IrO$_x$-untemplate	400	1.38	3.6	100	7.2	100	
IrO$_x$-untemplate	450	0.71	1.8	100	3.7	100	
IrO$_x$-untemplate	500	0.26	0.7	100	1.4	100	

[a] F.E.$_{O_2}$ is faradaic efficiency for O$_2$ evolution. [b] n_{H_2} is the amount of H$_2$ evolved in the Pt counter electrode compartment during the electrocatalysis. [c] F.E.$_{H_2}$ is faradaic efficiency for H$_2$ evolution. [d] R_{mes} is defined as the ratio of the amounts (n_{O_2}) of O$_2$ evolved for IrO$_x$-F127 and IrO$_x$-untemplate at corresponding calcination temperatures. [e] 2nd trial after the first bulk electrolysis. [f] 3rd trial after the second bulk electrolysis.

Conclusions

A new transparent mesoporous IrO_x electrocatalyst film consisting of an assembly of small interconnected nanoparticles (*ca.* 2–5 nm) has been achieved by a sustainable approach with very low iridium usage. A low concentrated Ir-precursor complex solution derived from polymer surfactant Pluronic F127 was simply drop-cast over FTO electrodes and then annealed at 400 °C to yield a stably adherent mesoporous film of amorphous IrO_x that works efficiently for electrocatalytic water oxidation. The higher performance of the present mesoporous IrO_x-F127 film for electrocatalytic water oxidation compared with the IrO_x-untemplate electrode was due to the increase of the intrinsic activity of the Ir-sites and faster electron transport through interconnected nanoparticles of the novel mesoporous network. This is a contrast to the case of the previous 2D-hexagonal mesoporous IrO_x system, in which the performance of electrocatalytic water oxidation was increased by the increase of the number of Ir-sites. The catalytic current for water oxidation with respect to the iridium amount (I_{cat}/Γ_{cov}) for the mesoporous IrO_x-F127 film was 5.3 and 4.3 times higher than those of the transparent efficient electrocatalyst films of the hitherto-reported 2D-hexagonal mesoporous IrO_x and nanoparticle $IrO_x(OH)_y$, respectively. The present transparent mesoporous IrO_x film is expected to be in great demand in artificial photosynthesis technology because of the simple and facile preparation procedure to obtain a highly active electrocatalyst with very low iridium amount.

Conflicts of interest

The authors declare no competing financial interests.

Acknowledgements

Notes and references

1 N. S. Lewis and D. G. Nocera, *Proc. Natl. Acad. Sci. U. S. A.*, 2006, **103**, 15729–15735.

2 T. R. Cook, D. K. Dogutan, S. Y. Reece, Y. Surendranath, T. S. Teets and D. G. Nocera, *Chem. Rev.*, 2010, **110**, 6474–6502.

3 S. Dahl and I. Chorkendorff, *Nat. Mater.*, 2012, **11**, 100–101.

4 H. Dotan, K. Sivula, M. Gratzel, A. Rothschild and S. C. Warren, *Energy Environ. Sci.*, 2011, **4**, 958–964.

5 M. Higashi, K. Domen and R. Abe, *J. Am. Chem. Soc.*, 2013, **135**, 10238–10241.

6 T. Hisatomi, H. Dotan, M. Stefik, K. Sivula, A. Rothschild, M. Grätzel and N. Mathews, *Adv. Mater.*, 2012, **24**, 2699–2702.

7 D. Chandra, K. Saito, T. Yui and M. Yagi, *ACS Sustainable Chem. Eng.*, 2018, **6**, 16838–16846.

8 A. J. Esswein, Y. Surendranath, S. Y. Reece and D. G. Nocera, *Energy Environ. Sci.*, 2011, **4**, 499–504.

9 A. Marshall, B. Børresen, G. Hagen, M. Tsypkin and R. Tunold, *Energy*, 2007, **32**, 431–436.

10 H. S. Ahn and T. D. Tilley, *Adv. Funct. Mater.*, 2013, **23**, 227–233.

11 M. W. Kanan and D. G. Nocera, *Science*, 2008, **321**, 1072–1075.

12 R. Takeuchi, T. Sato, K. Tanaka, K. Aiso, D. Chandra, K. Saito, T. Yui and M. Yagi, *ACS Appl. Mater. Interfaces*, 2017, **9**, 36955–36961.

13 C. C. L. McCrory, S. Jung, J. C. Peters and T. F. Jaramillo, *J. Am. Chem. Soc.*, 2013, **135**, 16977–16987.

14 L. Duan, F. Bozoglian, S. Mandal, B. Stewart, T. Privalov, A. Llobet and L. Sun, *Nat. Chem.*, 2012, **4**, 418–423.

15 K. S. Joya, Y. F. Joya, K. Ocakoglu and R. van de Krol, *Angew. Chem., Int. Ed.*, 2013, **52**, 10426–10437.

16 X. Sala, I. Romero, M. Rodríguez, L. Escriche and A. Llobet, *Angew. Chem., Int. Ed.*, 2009, **48**, 2842–2852.

17 K. S. Joya, N. K. Subbaiyan, F. D'Souza and H. J. M. de Groot, *Angew. Chem., Int. Ed.*, 2012, **51**, 9601–9605.

18 T. Nakagawa, N. S. Bjorge and R. W. Murray, *J. Am. Chem. Soc.*, 2009, **131**, 15578–15579.

19 M. M. Najafpour, T. Ehrenberg, M. Wiechen and P. Kurz, *Angew. Chem., Int. Ed.*, 2010, **49**, 2233–2237.

20 Y. Gorlin and T. F. Jaramillo, *J. Am. Chem. Soc.*, 2010, **132**, 13612–13614.

21 C. Hammond, M. T. Schümperli and I. Hermans, *Chem.–Eur. J.*, 2013, **19**, 13193–13198.

22 M. Moser, C. Mondelli, A. P. Amrute, A. Tazawa, D. Teschner, M. E. Schuster, A. Klein-Hoffman, N. López, T. Schmidt and J. Pérez-Ramírez, *ACS Catal.*, 2013, **3**, 2813–2822.

23 L.-M. Kuo, Y.-C. Chou, K.-N. Chen, C.-C. Lu and S. Chao, *Sens. Actuators, B*, 2014, **193**, 687–691.

24 Y. Lee, M. Kang, J. H. Shim, N.-S. Lee, J. M. Baik, Y. Lee, C. Lee and M. H. Kim, *J. Phys. Chem. C*, 2012, **116**, 18550–18556.

25 J. H. Shim, Y. Lee, M. Kang, J. Lee, J. M. Baik, Y. Lee, C. Lee and M. H. Kim, *Anal. Chem.*, 2012, **84**, 3827–3832.

26 R.-T. Wen, G. A. Niklasson and C. G. Granqvist, *Sol. Energy Mater. Sol. Cells*, 2014, **120**(Part A), 151–156.

27 D.-Q. Liu, S.-H. Yu, S.-W. Son and S.-K. Joo, *Electrochem. Solid-State Lett.*, 2008, **11**, A206–A208.

28 Y. Zhao, N. M. Vargas-Barbosa, E. A. Hernandez-Pagan and T. E. Mallouk, *Small*, 2011, 7, 2087–2093.

29 Y. Zhao, E. A. Hernandez-Pagan, N. M. Vargas-Barbosa, J. L. Dysart and T. E. Mallouk, *J. Phys. Chem. Lett.*, 2011, **2**, 402–406.

30 T. Kuwabara, E. Tomita, S. Sakita, D. Hasegawa, K. Sone and M. Yagi, *J. Phys. Chem. C*, 2008, **112**, 3774–3779.

31 M. Yagi, E. Tomita, S. Sakita, T. Kuwabara and K. Nagai, *J. Phys. Chem. B*, 2005, **109**, 21489–21491.

32 M.-C. Chuang and J.-a. A. Ho, *RSC Adv.*, 2012, **2**, 4092–4096.

33 D. Chandra, D. Takama, T. Masaki, T. Sato, N. Abe, T. Togashi, M. Kurihara, K. Saito, T. Yui and M. Yagi, *ACS Catal.*, 2016, **6**, 3946–3954.

34 T. Nakagawa, C. A. Beasley and R. W. Murray, *J. Phys. Chem. C*, 2009, **113**, 12958–12961.

35 E. N. El Sawy and V. I. Birss, *J. Mater. Chem.*, 2009, **19**, 8244–8252.

36 G. Li, H. Yu, W. Song, M. Dou, Y. Li, Z. Shao and B. Yi, *ChemSusChem*, 2012, **5**, 858–861.

37 E. Ortel, T. Reier, P. Strasser and R. Kraehnert, *Chem. Mater.*, 2011, **23**, 3201–3209.

38 M. Bernicke, E. Ortel, T. Reier, A. Bergmann, J. Ferreira de Araujo, P. Strasser and R. Kraehnert, *ChemSusChem*, 2015, **8**, 1908–1915.

39 D. Chandra, N. Abe, D. Takama, K. Saito, T. Yui and M. Yagi, *ChemSusChem*, 2015, **8**, 795–799.

40 D. Chandra, T. Sato, R. Takeuchi, D. Li, T. Togashi, M. Kurihara, K. Saito, T. Yui and M. Yagi, *Catal. Today*, 2017, **290**, 51–58.

41 W. Hu, Y. Wang, X. Hu, Y. Zhou and S. Chen, *J. Mater. Chem.*, 2012, **22**, 6010–6016.

42 W. J. Youngblood, S.-H. A. Lee, Y. Kobayashi, E. A. Hernandez-Pagan, P. G. Hoertz, T. A. Moore, A. L. Moore, D. Gust and T. E. Mallouk, *J. Am. Chem. Soc.*, 2009, **131**, 926–927.

43 S. D. Tilley, M. Cornuz, K. Sivula and M. Grätzel, *Angew. Chem., Int. Ed.*, 2010, **49**, 6405–6408.

44 M. Hara and T. E. Mallouk, *Chem. Commun.*, 2000, 1903–1904.

45 R. D. L. Smith, B. Sporinova, R. D. Fagan, S. Trudel and C. P. Berlinguette, *Chem. Mater.*, 2014, **26**, 1654–1659.

46 P. G. Hoertz, Y.-I. Kim, W. J. Youngblood and T. E. Mallouk, *J. Phys. Chem. B*, 2007, **111**, 6845–6856.

47 M. Yagi, E. Tomita and T. Kuwabara, *J. Electroanal. Chem.*, 2005, **579**, 83–88.

48 M. A. Petit and V. Plichon, *J. Electroanal. Chem.*, 1998, **444**, 247–252.

49 Z. Wu, Q. Li, D. Feng, P. A. Webley and D. Zhao, *J. Am. Chem. Soc.*, 2010, **132**, 12042–12050.

50 B. T. Holland, C. F. Blanford and A. Stein, *Science*, 1998, **281**, 538–540.

51 C. Sanchez, C. Boissière, D. Grosso, C. Laberty and L. Nicole, *Chem. Mater.*, 2008, **20**, 682–737.

52 D. Chandra, T. Ohji, K. Kato and T. Kimura, *Langmuir*, 2011, **27**, 11436–11443.

53 Y.-J. Cheng, L. Zhi, W. Steffen and J. S. Gutmann, *Chem. Mater.*, 2008, **20**, 6580–6582.

54 D. Chandra, T. Ohji, K. Kato and T. Kimura, *Phys. Chem. Chem. Phys.*, 2011, **13**, 12529–12535.

55 X. Meng, T. Kimura, T. Ohji and K. Kato, *J. Mater. Chem.*, 2009, **19**, 1894–1900.

56 D. Chandra, S. K. Das and A. Bhaumik, *Microporous Mesoporous Mater.*, 2010, **128**, 34–40.

57 S. S. Thanawala, R. J. Baird, D. G. Georgiev and G. W. Auner, *Appl. Surf. Sci.*, 2008, **254**, 5164–5169.

58 Y.-M. Chen, J.-H. Cai, Y.-S. Huang, K.-Y. Lee, D.-S. Tsai and K.-K. Tiong, *Thin Solid Films*, 2012, **520**, 2409–2413.

59 Y. S. Huang, S. S. Lin, C. R. Huang, M. C. Lee, T. E. Dann and F. Z. Chien, *Solid State Commun.*, 1989, **70**, 517–522.

60 P. C. Liao, C. S. Chen, W. S. Ho, Y. S. Huang and K. K. Tiong, *Thin Solid Films*, 1997, **301**, 7–11.

61 S. Zou, H. Y. H. Chan, C. T. Williams and M. J. Weaver, *Langmuir*, 1999, **16**, 754–763.

62 A. C. Ferrari and J. Robertson, *Phys. Rev. B: Condens. Matter Mater. Phys.*, 2000, **61**, 14095–14107.

63 D. Chandra, K. Saito, T. Yui and M. Yagi, *Angew. Chem., Int. Ed.*, 2013, **52**, 12606–12609.

64 D. Zhao, P. Yang, N. Melosh, J. Feng, B. F. Chmelka and G. D. Stucky, *Adv. Mater.*, 1998, **10**, 1380–1385.

65 A. Grosman and C. Ortega, *Langmuir*, 2008, **24**, 3977–3986.

66 P. Yang, D. Zhao, D. I. Margolese, B. F. Chmelka and G. D. Stucky, *Chem. Mater.*, 1999, **11**, 2813–2826.

67 E. Rasten, G. Hagen and R. Tunold, *Electrochim. Acta*, 2003, **48**, 3945–3952.

68 J.-M. Hu, J.-Q. Zhang and C.-N. Cao, *Int. J. Hydrogen Energy*, 2004, **29**, 791–797.

69 E. Guerrini, H. Chen and S. Trasatti, *J. Solid State Electrochem.*, 2007, **11**, 939–945.